The bohmion method in nonadiabatic molecular dynamics

Darryl D. Holm[1], Jonathan I. Rawlinson[2], Cesare Tronci[3,4]

[1]*Department of Mathematics, Imperial College London, London, UK*

[2]*School of Mathematics, University of Bristol, Bristol, UK*

[3]*Department of Mathematics, University of Surrey, Guildford, UK*

[4]*Department of Physics and Engineering Physics, Tulane University, New Orleans LA, USA*

Abstract

Starting with the exact factorization of the molecular wavefunction, this paper presents the results from the numerical implementation in *ab-initio* nonadiabatic dynamics of the recently proposed bohmion method. Within the context of quantum hydrodynamics, the regularized nuclear Bohm potential in the bohmion method admits solutions comprising a train of $\delta-$functions which serve as a finite-dimensional sampling of the hydrodynamic flow paths. In addition, the nonlocal structure of the regularized Bohm potential admits nuclear quantum tunneling events. After reviewing the general theory, the bohmion method is applied to the well-known Tully models, which are used here as benchmark problems for the comparison of the new bohmion method with previous mixed quantum-classical methods.

Contents

1 Introduction

1.1 *Ab-initio* methods in nonadiabatic dynamics

Since the appearance of the surface-hopping method in the early 70's [51], the increasing availability of computational power has enabled a series of different approaches for simulation of nonadiabatic systems in quantum molecular dynamics. In this context, the nuclear response to the quantum electronic transitions poses major challenges, since the mean-field approximation is generally unable to capture such effects accurately. In addition, both the mean-field model and the surface-hopping method often fail to adequately describe electronic decoherence, even though several corrections have been proposed over the years [37, 19, 44]. All these difficulties in capturing the various features of vibronic interactions are related to the long-standing problem of quantum-classical coupling [3, 7, 17, 29, 45].

Mixed quantum-classical approaches are often based on the Born-Huang expansion [9] of the molecular wavefunction. This type of approach introduces nuclear trajectories by projecting the time-dependent expansion coefficients on a basis set of frozen Gaussian wavepackets [20, 28]. Prominent examples are the multiconfigurational Ehrenfest method [41], multiple spawning [5] and, more recently, multiple cloning [33]. Alternatively, the nuclear coefficients have also been approached in terms of Bohmian trajectories within the framework of quantum hydrodynamics [38, 47]. Such approaches, in principle, would allow for description of quantum nuclear effects such as tunneling [13] and zero-point energy [18] due to the quantum nature of Bohmian trajectories.

Recently, new perspectives have emerged in the context of the exact wavefunction factorization [1, 2]. Instead of focusing on the Born-Huang series expansion, this picture involves an alternative representation of the molecular wavefunction, expressed as follows:

$$\Psi(\boldsymbol{r}, \boldsymbol{x}, t) = \chi(\boldsymbol{r}, t)\phi(\boldsymbol{x}, t; \boldsymbol{r}) \qquad \text{with} \qquad \int |\phi(\boldsymbol{x}, t; \boldsymbol{r})|^2 \, \mathrm{d}^3 x = 1 \,. \tag{1}$$

The electronic function $\phi(\boldsymbol{x}, t; \boldsymbol{r})$ is taken to be square-integrable in the electronic coordinates $\boldsymbol{x}$ while it is parameterized by the nuclear coordinate $\boldsymbol{r}$. Although this representation is reminiscent of the adiabatic Born-Oppenheimer (BO) theory, here the electronic function depends explicitly on time. The representation of the wavefunction in (1) was first considered several decades ago [21] (see also Section 11.1 in [6]), although its advantages in nonadiabatic dynamics have apparently not been recognized until much more recently. In the paper [4], the representation (1) was combined with quantum hydrodynamics and the Born-Huang expansion to formulate a *coupled-trajectory mixed-quantum-classical method* (CT-MQC) which showed promising results.

In the present paper, we consider an alternative approach which combines the hydrodynamic form of the exact factorization representation (1) with suitable closure ansatzes that are made possible by an appropriate regularization of the quantum potential. Based on the variational principle underlying quantum hydrodynamics, we perform a regularization of the probability density so that the latter can be represented by a train of $\delta-$functions called *bohmions*, whose interactions mimic the trajectories of point particles. However, the finite-dimensional bohmion closure also retains quantum effects inherited from the presence of the regularized quantum potential. The bohmion closure partially applies a singular momentum map from geometric mechanics [23, 25] which is dual to the standard Madelung transformation of quantum mechanics [31, 32] into the language of hydrodynamics. First formulated in [15], this method reveals

the Lagrangian-particle content of quantum hydrodynamics. Namely, the singular bohmions follow Lagrangian flow trajectories in quantum hydrodynamics.

The content of the paper is as follows. In the remainder of Section 1 we summarise the main points of the derivation of the bohmion model. In particular, one sets up the variational principle underlying standard quantum hydrodynamics before applying the bohmion method to yield the equations of motion for nuclear bohmions. In Section 2 we outline the extension of these ideas to nonadiabatic molecular dynamics [15]. First, the hydrodynamic formulation of the exact factorization representation is described along with its variational structure. In Section 2.3 the bohmion method is applied within this context, leading to the bohmion equations for nonadiabatic dynamics. These equations are the starting point for the numerical simulations which follow. Section 3 contains new results from the numerical implementation of the bohmion method to the celebrated Tully models [49], with a focus on population transfer and decoherence dynamics. On the whole, these numerical implementations display excellent agreement with exact quantum mechanical results. In particular, they show that bohmions are able to capture electronic decoherence effects in a variety of nonadiabatic processes. Comparisons are also made with other methods, including CT-MQC [4]. Section 4 contains our conclusions.

1.2   The bohmion method in quantum hydrodynamics

Before entering the details of how the bohmion method applies to nonadiabatic molecular dynamics, let us illustrate how bohmions emerge in standard quantum hydrodynamics (QHD). Upon using the Madelung transform $\chi(\boldsymbol{r}) = \sqrt{D}e^{iS/\hbar}$ and denoting $\boldsymbol{u} = \nabla S/M$, the QHD equations read [15]

$$M(\partial_t + \boldsymbol{u} \cdot \nabla)\boldsymbol{u} = -\nabla(V_Q + V), \qquad\qquad \partial_t D + \operatorname{div}(D\boldsymbol{u}) = 0, \qquad (2)$$

where V is an external potential and M denotes the mass. The quantity in (2)

$$V_Q = -\frac{\hbar^2}{2M}\frac{\Delta\sqrt{D}}{\sqrt{D}}$$

is the celebrated quantum potential.

The Lagrange-to-Euler map for the probability density D in QHD is given in terms of the initial condition $D_0(\boldsymbol{r}_0)$ by

$$D(\boldsymbol{r}, t) = \int D_0(\boldsymbol{r}_0)\delta(\boldsymbol{r} - \boldsymbol{\eta}(\boldsymbol{r}_0, t))\,\mathrm{d}^3 r_0. \qquad (3)$$

A vector calculus exercise shows that the density transport equation in (2) is recovered by taking the time derivative of the Lagrange-to-Euler map in (3). The Lagrangian fluid map $\boldsymbol{\eta}$ in (3) plays a crucial role in the hydrodynamic interpretation of equations (2). In fact, the hydrodynamic velocity $\boldsymbol{u}(\boldsymbol{r}, t)$ in (2) is defined as the tangent vector to the Bohmian trajectory $\boldsymbol{\eta}(\boldsymbol{r}_0, t)$ given by

$$\dot{\boldsymbol{\eta}}(\boldsymbol{r}_0, t) := \partial_t\boldsymbol{\eta}(\boldsymbol{r}_0, t) = \boldsymbol{u}(\boldsymbol{\eta}(\boldsymbol{r}_0, t), t). \qquad (4)$$

Thus, the Bohmian trajectory identifies the evolution of Lagrangian fluid parcels labelled by their initial nuclear position $\boldsymbol{r}_0$ and moving with velocity $\boldsymbol{u}(\boldsymbol{\eta}(\boldsymbol{r}_0, t), t)$.

To illustrate the bohmion method, we will exploit the variational principle for the QHD equations (2). Indeed, the latter arise from the variational principle

$$\delta \int_{t_1}^{t_2} \int \left(MD\frac{|\boldsymbol{u}|^2}{2} - \frac{\hbar^2}{8M}\frac{|\nabla D|^2}{D} - DV \right) \mathrm{d}^3 r\,\mathrm{d}t = 0, \qquad (5)$$

where the variations δD and $\delta \boldsymbol{u}$ arise from the relations (3)-(4). Upon composing (4) by the inverse variable $\boldsymbol{\eta}^{-1}$, the resulting relation $\boldsymbol{u}(\boldsymbol{r}, t) = \dot{\boldsymbol{\eta}}(\boldsymbol{r}_0, t)|_{\boldsymbol{r}_0 = \boldsymbol{\eta}^{-1}(\boldsymbol{r}, t)}$ leads to

$$\delta \boldsymbol{u} = \partial_t \boldsymbol{w} + (\boldsymbol{u} \cdot \nabla) \boldsymbol{w} - (\boldsymbol{w} \cdot \nabla) \boldsymbol{u}, \qquad \delta D = -\operatorname{div}(D\boldsymbol{w}). \qquad (6)$$

Here, we have introduced $\boldsymbol{w}(\boldsymbol{r}, t) = \delta \boldsymbol{\eta}(\boldsymbol{r}_0, t)|_{\boldsymbol{r}_0 = \boldsymbol{\eta}^{-1}(\boldsymbol{r}, t)}$ and the variation δD follows from the relation (3). The reduction from Lagrangian/Bohmian variables to Eulerian variables in Hamilton's principle for ideal fluid dynamics is called Euler-Poincaré reduction [24]. See [16] for an extension to include the presence of hydrodynamic vortices in QHD.

In the absence of the quantum potential in (2), we realize that the point particle solution $D(\boldsymbol{r}, t) = \delta(\boldsymbol{r} - \boldsymbol{q}(t))$ of the transport equation is compatible with the fluid momentum equation. This recovers Newton's law $M\ddot{\boldsymbol{q}} = \nabla V(\boldsymbol{q})$. However, the same cannot be said in the presence of the quantum potential term, which requires the density to be continuous and differentiable. The bohmion method [15] overcomes this difficulty by inserting a *mollifier* $K(\boldsymbol{r} - \boldsymbol{r}')$, so that the regularized probability density $\bar{D}(\boldsymbol{r}, t) = \int K(\boldsymbol{r} - \boldsymbol{r}') D(\boldsymbol{r}', t) \, \mathrm{d}^3 r$ is made available. A similar approach was recently applied to regularize conical intersections in adiabatic dynamics with geometric phase effects [40]. The mollifier is typically rotation-invariant and depends on a lengthscale parameter α so that the limit $\alpha \to 0$ returns the original hydrodynamic variable D. For example, α could be the width of a Gaussian convolution. At this point, the QHD variational principle (5) is modified to read

$$\delta \int_{t_1}^{t_2} \int \left(MD\frac{|\boldsymbol{u}|^2}{2} - \frac{\hbar^2}{8M} \frac{|\nabla \bar{D}|^2}{\bar{D}} - DV \right) \mathrm{d}^3 r \, \mathrm{d}t = 0. \qquad (7)$$

Without finding the explicit equations of motion, the bohmion method proceeds by substituting the point particle ansatz

$$D(\boldsymbol{r}, t) = \sum_{a=1}^{N} w_a \delta(\boldsymbol{r} - \boldsymbol{q}_a(t)), \qquad (8)$$

with $w_a > 0$ and $\sum_a w_a = 1$. Here, N is a number of bohmions that is chosen depending on the desired accuracy; further comments on this point will be provided in the following sections. Here, we notice that the ansatz (8) comprises part of a momentum map structure which has already appeared in geometric mechanics within a different context [25].

Insertion of (8) into the transport equation yields $\dot{\boldsymbol{q}}_a = \boldsymbol{u}(\boldsymbol{q}_a)$, and then substitution into the variational principle (7) leads to the following finite dimensional variational principle

$$\delta \int_{t_1}^{t_2} \sum_a w_a \left(M\frac{|\dot{\boldsymbol{q}}_a|^2}{2} - V(\boldsymbol{q}_a) - \sum_b \frac{\hbar^2 w_b}{8M} \int \frac{\nabla K(\boldsymbol{r}' - \boldsymbol{q}_a) \cdot \nabla K(\boldsymbol{r}' - \boldsymbol{q}_b)}{\sum_c w_c K(\boldsymbol{r}' - \boldsymbol{q}_c)} \, \mathrm{d}^3 r' \right) \mathrm{d}t = 0, \qquad (9)$$

where all the sums run from 1 to N.

At this point, the problem has been made finite-dimensional and the bohmion motion is governed by the Euler-Lagrange equations for $\boldsymbol{q}_a$. Notice that the regularized quantum potential term in (9) is not a classical interaction potential. Indeed, this term retains quantum nonlocal effects, since it depends on all of the bohmion locations. This nonlocal quantum dependence results in a modification of the external potential and thereby admits quantum effects such as tunneling and zero-point energy. In addition, as bohmion dynamics is Hamiltonian, it naturally inherits conservation of energy and momentum.

Based on the hydrodynamic formulation of the exact wavefunction factorization from Section 2.1, this method will now be applied to the general problem of nonadiabatic molecular dynamics.

2 The bohmion method in nonadiabatic dynamics

2.1 Exact wavefunction factorization

In this section, we present some generalities on the hydrodynamic formulation of the exact factorization representation (1). This will be useful for the subsequent discussions.

Without loss of generality, here we restrict to consider the case of a three-dimensional nuclear coordinate $\boldsymbol{r}$ and a three-dimensional electronic coordinate $\boldsymbol{x}$. The extension to several nuclei and electrons is straightforward. As usual, the Hamiltonian operator $\widehat{H} = \widehat{T}_n + \widehat{H}_e$ is written as the sum of the nuclear kinetic energy $\widehat{T}_n = -M^{-1}\hbar^2\Delta_{\boldsymbol{r}}/2$ and the electronic Hamiltonian $\widehat{H}_e = \widehat{H}_e(\boldsymbol{r})$ containing the interaction terms. Upon using the Madelung transform $\chi = \sqrt{D}e^{iS/\hbar}$, one writes nuclear dynamics in the hydrodynamic form

$$M(\partial_t + \boldsymbol{u} \cdot \nabla)\boldsymbol{u} = -\nabla(V_Q + \epsilon) - \boldsymbol{E} - \boldsymbol{u} \times \boldsymbol{B}, \tag{10}$$

$$\partial_t D + \operatorname{div}(D\boldsymbol{u}) = 0. \tag{11}$$

Here, all differential operators are defined on the nuclear coordinate space and the notation is as follows: $\boldsymbol{A} = \langle\phi| - i\hbar\nabla\phi\rangle$ is the Berry connection with curvature $\boldsymbol{B} = \operatorname{curl}\boldsymbol{A}$, while $\boldsymbol{u} = M^{-1}(\nabla S + \boldsymbol{A})$ is the hydrodynamic velocity. Also, ϵ is the effective electronic potential

$$\epsilon(\phi, \nabla\phi) := \langle\phi|\widehat{H}_e\phi\rangle + \frac{\hbar^2}{2M}\|\nabla\phi\|^2 - \frac{\boldsymbol{A}^2}{2M},$$

where we have used the notation $\langle\phi_1|\phi_2\rangle = \int \phi_1^*\phi_2 \, \mathrm{d}^3x$ and $\|\phi_1\|^2 = \int |\phi_1|^2 \mathrm{d}^3x$. Finally, $\boldsymbol{E} = -\partial_t\boldsymbol{A} - \nabla\langle\phi|i\hbar\partial_t\phi\rangle$. Then, the electronic Schrödinger equation can be written as follows:

$$i\hbar\partial_t\phi + i\hbar(\boldsymbol{u} - M^{-1}\boldsymbol{A}) \cdot \nabla\phi = \widehat{H}_e\phi - \frac{\hbar^2}{2MD}\operatorname{div}(D\nabla\phi) + \lambda\phi, \tag{12}$$

where $\lambda(\boldsymbol{r}, t)$ is a function depending on the gauge choice on $\langle\phi|i\hbar\partial_t\phi\rangle$. Equations (10), (11), and (12) comprise the hydrodynamic formulation of the exact factorization system in [15, 46]. Combined with the Born-Huang expansion, this system is the basis for the new *coupled-trajectory mixed-quantum-classical method* (CT-MQC) in nonadiabatic molecular dynamics [4].

2.2 Variational structure

In order to prepare the framework for the formulation of the bohmion method, here we illustrate the variational structure of the hydrodynamic formulation of the exact factorization system. This will be a basic ingredient for introducing the bohmions in the next section.

Before introducing the variational structure, we choose to rewrite the system (10), (11), and (12) in a slightly different form. First, after some algebraic manipulations [15], we notice that

$$\boldsymbol{E} = -\boldsymbol{u} \times \boldsymbol{B} - \nabla\epsilon + \langle\phi|(\nabla\widehat{H}_e)\phi\rangle + \frac{1}{MD}\operatorname{div}(D\mathbb{T}).$$

Here, $\mathbb{T} = \operatorname{Re}\mathbb{Q}$ denotes the real part of the *quantum geometric tensor* $\mathbb{Q}_{jk} = \langle\partial_j\phi|\partial_k\phi\rangle - \hbar^{-2}A_jA_k$ [39]. By using the relation above, equation (10) becomes

$$M(\partial_t + \boldsymbol{u} \cdot \nabla)\boldsymbol{u} = -\nabla V_Q - \langle\phi|(\nabla\widehat{H}_e)\phi\rangle - \frac{1}{MD}\operatorname{div}(D\mathbb{T}). \tag{13}$$

Also, we notice that the electronic equation (12) can be rewritten as

$$i\hbar\partial_t\phi + i\hbar\boldsymbol{u}\cdot\nabla\phi = \widehat{H}_e\phi + \frac{\hbar^2}{4MD}\frac{\delta F}{\delta\phi} + \lambda\phi\,.$$

In the above we have introduced $F = \int D\,\mathrm{Tr}\,\mathbb{T}\,\mathrm{d}^3r$, where Tr denotes the matrix trace. Then, upon writing $T = \mathrm{Tr}\,\mathbb{T}$, the functional derivative of F is $\delta F/\delta\phi = D\partial T/\partial\phi - \mathrm{div}(D\partial T/\partial\nabla\phi)$.

At this point, we use the density matrix $\rho(\boldsymbol{x},\boldsymbol{x}',t;\boldsymbol{r}) = \phi(\boldsymbol{x},t;\boldsymbol{r})\phi(\boldsymbol{x}',t;\boldsymbol{r})^*$ to write $\mathbb{T}_{jk} = \langle\partial_j\rho|\partial_k\rho\rangle$ and $F = \int D\|\nabla\rho\|^2/2\,\mathrm{d}^3r$ where we have used the notation $\langle\rho_1|\rho_2\rangle = \int\rho_1(\boldsymbol{x}',\boldsymbol{x})^*\rho_2(\boldsymbol{x},\boldsymbol{x}')\,\mathrm{d}^3x\,\mathrm{d}^3x'$ and $\|\nabla\rho\|^2 = \langle\partial_k\rho|\partial_k\rho\rangle$. Then, we notice that the chain rule ensures $\delta F/\delta\phi = 2(\delta F/\delta\rho)\phi$ so that the electronic Schrödinger equation (12) can be written as the quantum Liouville equation

$$i\hbar\left(\frac{\partial}{\partial t} + \boldsymbol{u}\cdot\nabla\right)\rho + \left[\rho,\widehat{H}_e\right] = \frac{\hbar^2}{2MD}\left[\frac{\delta F}{\delta\rho},\rho\right] = \frac{\hbar^2}{2MD}\,\mathrm{div}\left(D\left[\rho,\nabla\rho\right]\right)\,, \qquad (14)$$

where we have used $\delta F/\delta\rho = -\,\mathrm{div}(D\nabla\rho)$ and we have applied the Leibniz rule. Here, we notice the emergence of the quantity $[\rho,\nabla\rho]$: as recognized in [36], this is a type of non-Abelian gauge connection. See [14] for recent advances on the appearance of non-Abelian gauge connections in nonadiabatic dynamics. It will be convenient to introduce the variable $\tilde{\rho} = D\rho$. Then, eventually the equations of motion become

$$MD(\partial_t + \boldsymbol{u}\cdot\nabla)\boldsymbol{u} = D\nabla V_Q - \langle\tilde{\rho}|\nabla\widehat{H}_e\rangle + \frac{\hbar^2}{2M}\partial_j\langle\tilde{\rho},\nabla(D^{-1}\partial_j\tilde{\rho})\rangle\,, \qquad (15)$$

$$\partial_t D + \mathrm{div}(D\boldsymbol{u}) = 0\,, \qquad (16)$$

$$i\hbar\partial_t\tilde{\rho} + i\hbar\,\mathrm{div}(\tilde{\rho}\boldsymbol{u}) = \left[\widehat{H}_e,\tilde{\rho}\right] + \frac{\hbar^2}{2M}\,\mathrm{div}\left(D^{-1}\left[\tilde{\rho},\nabla\tilde{\rho}\right]\right)\,. \qquad (17)$$

These equations comprise the general description of nonadiabatic quantum hydrodynamics. First appearing in [15], it was shown that they possess both a Hamiltonian and variational formulation. The latter is particularly important as it allows application of the bohmion method explained previously.

The Euler-Poincaré variational principle $\delta\int_{t_1}^{t_2}\ell\,\mathrm{d}t = 0$ for nonadiabatic quantum hydrodynamics involves the Lagrangian

$$\ell(\boldsymbol{u},D,\xi,\rho) = \int\left[\frac{1}{2}MD|\boldsymbol{u}|^2 - \frac{\hbar^2}{8M}\frac{(\nabla D)^2}{D} + \langle\tilde{\rho}|i\hbar\xi - \widehat{H}_e\rangle - \frac{\hbar^2 D}{4M}\left\|\nabla\left(\frac{\tilde{\rho}}{D}\right)\right\|^2\right]\mathrm{d}^3r\,. \qquad (18)$$

The presence of the density matrix in Hamilton's variational principle is treated here by using the techniques first developed in [8, 48]. In this case, the evolution of the density matrix density $\tilde{\rho}$ requires some discussion. Usually, the quantum density matrix evolves according to $\rho_0 \mapsto U(t)\rho_0 U(t)^\dagger$, where $U(t)$ is the unitary propagator. In the present case, we recall that $\rho(\boldsymbol{r},t)$ retains parametric dependence on the nuclear coordinates and thus so does the unitary propagator, which we shall denote by $U(\boldsymbol{r},t)$. In addition, the electronic density matrix ρ evolves in the frame of the nuclear fluid as indicated by the convective time derivative in the left-hand side of (14). Then, the density matrix density $\tilde{\rho} = D\rho$ evolves according to [15]

$$\tilde{\rho} = \int\hat{\rho}(\boldsymbol{r}_0,t)\,\delta(r - \eta(\boldsymbol{r}_0,t))\,\mathrm{d}^3r_0\,, \qquad \text{with} \qquad \hat{\rho}(\boldsymbol{r}_0,t) = U(\boldsymbol{r}_0,t)\tilde{\rho}_0(\boldsymbol{r}_0)U^\dagger(\boldsymbol{r}_0,t)\,. \qquad (19)$$

In terms of these variables, the quantum generator of motion $\xi(\boldsymbol{r}, t)$ is defined as $\xi(\boldsymbol{r}, t) = \dot{U}(\boldsymbol{r}_0, t)U(\boldsymbol{r}_0, t)^\dagger|_{\boldsymbol{r}_0 = \boldsymbol{\eta}^{-1}(\boldsymbol{r}, t)}$, so that equation (17) has the general structure $\partial_t \tilde{\rho} + \mathrm{div}(\tilde{\rho}\boldsymbol{u}) = [\xi, \tilde{\rho}]$. Also, upon denoting $\nu(\boldsymbol{r}, t) = \delta U(\boldsymbol{r}_0, t)U(\boldsymbol{r}_0, t)^\dagger|_{\boldsymbol{r}_0 = \boldsymbol{\eta}^{-1}(\boldsymbol{r}, t)}$, one obtains the variational relations $\delta\tilde{\rho} = [\nu, \tilde{\rho}] - \mathrm{div}(\boldsymbol{w}\tilde{\rho})$ and $\delta\xi = \partial_t\nu - \boldsymbol{w} \cdot \nabla\xi + \boldsymbol{u} \cdot \nabla\nu - [\xi, \nu]$, while $\boldsymbol{w}$ and all other variations are as in (6).

2.3 The bohmion method

In the construction above, the density matrix density $\tilde{\rho}$ needs to be accommodated to fit the bohmion method introduced in Section 1.2. We do this by defining the regularized density matrix density $\bar{\rho}(\boldsymbol{r}, t) = \int K(\boldsymbol{r} - \boldsymbol{r}')\tilde{\rho}(\boldsymbol{r}', t)\,\mathrm{d}^3 r$ alongside $\bar{D}(\boldsymbol{r}, t) = \int K(\boldsymbol{r} - \boldsymbol{r}')D(\boldsymbol{r}', t)\,\mathrm{d}^3 r$. Then, we consider the following regularized version of the Lagrangian (18):

$$\ell = \int \left[\frac{1}{2}MD|\boldsymbol{u}|^2 - \frac{\hbar^2}{8M}\frac{(\nabla\bar{D})^2}{\bar{D}} + \langle\tilde{\rho}|i\hbar\xi - \widehat{H}_e\rangle - \frac{\hbar^2}{4M}\left\|\nabla\left(\frac{\bar{\rho}}{\bar{D}}\right)\right\|^2 \right]\mathrm{d}^3 r\,. \tag{20}$$

As explained in [15], replacing the the initial condition $\tilde{\rho}_0(\boldsymbol{r}_0) = \sum_a w_a \varrho_a^{(0)}\delta(\boldsymbol{r}_0 - \boldsymbol{q}_a^{(0)})$ in (19) leads to

$$\tilde{\rho}(\boldsymbol{r}, t) = \sum_a w_a \varrho_a(t)\delta(\boldsymbol{r} - \boldsymbol{q}_a(t))\,, \qquad \text{with} \qquad \varrho_a(t) := \mathcal{U}_a(t)\varrho_a^{(0)}\mathcal{U}_a(t)^\dagger\,. \tag{21}$$

Here, we have denoted $\mathcal{U}_a(t) := U(\boldsymbol{q}_a^{(0)}, t)$ and we set $\varrho_a^{(0)}(\boldsymbol{x}, \boldsymbol{x}') = \varphi_a^{(0)}(\boldsymbol{x})\varphi_a^{(0)}(\boldsymbol{x}')^*$, so that $\varrho_a(\boldsymbol{x}, \boldsymbol{x}', t) = \varphi_a(\boldsymbol{x}, t)\varphi_a(\boldsymbol{x}', t)^*$ at all times. Again, we notice that the ansatz (21) comprises part of a singular momentum map structure in geometric mechanics, as discussed in [25]. Then, using the ansatz (8) and denoting $\xi_a = \dot{\mathcal{U}}_a\mathcal{U}_a^\dagger$, one obtains the nonadiabatic bohmion Lagrangian

$$L(\{\boldsymbol{q}\}, \{\dot{\boldsymbol{q}}\}, \{\varrho\}) = \sum_a w_a \Bigg(\frac{M}{2}\dot{\boldsymbol{q}}_a^2 + \langle\varrho_a, i\hbar\xi_a - \widehat{H}_e(\boldsymbol{q}_a)\rangle$$
$$+ \frac{\hbar^2}{8M}\sum_b w_b(1 - 2\langle\varrho_a|\varrho_b\rangle)\int \frac{\nabla K(\boldsymbol{r} - \boldsymbol{q}_a) \cdot \nabla K(\boldsymbol{r} - \boldsymbol{q}_b)}{\sum_c w_c K(\boldsymbol{r} - \boldsymbol{q}_c)}\,\mathrm{d}^3 r \Bigg)\,. \tag{22}$$

As discussed in [15], Hamilton's principle $\delta \int_{t_1}^{t_2} L\,\mathrm{d}t = 0$ requires the variations

$$\delta\xi_a = \partial_t\nu_a - [\xi_a, \nu_a]\,, \qquad\qquad \delta\varrho_a = [\nu_a, \varrho_a]\,,$$

where $\nu_a = (\delta\mathcal{U}_a)\mathcal{U}_a^\dagger$. These relations are easily verified from the definitions of ξ_a and ϱ_a. Eventually, the bohmion motion is governed by the Euler-Lagrange equations for $\boldsymbol{q}_a$, which are accompanied by a sequence of quantum Liouville equations for ϱ_a. The latter read

$$i\hbar\dot{\varrho}_a = [\widehat{H}_e(\boldsymbol{q}_a), \varrho_a] + \frac{\hbar^2}{2M}\sum_b w_b[\varrho_b, \varrho_a]\int \frac{\nabla K(\boldsymbol{r} - \boldsymbol{q}_a) \cdot \nabla K(\boldsymbol{r} - \boldsymbol{q}_b)}{\sum_c w_c K(\boldsymbol{r} - \boldsymbol{q}_c)}\,\mathrm{d}^3 r\,. \tag{23}$$

Upon writing $\varrho_a(\boldsymbol{x}, \boldsymbol{x}', t) = \varphi_a(\boldsymbol{x}, t)\varphi(\boldsymbol{x}, t)^*$, we can also write the corresponding Schrödinger equation as follows:

$$i\hbar\dot{\varphi}_a = \widehat{H}_e(\boldsymbol{q}_a)\varphi_a + \frac{\hbar^2}{M}\sum_b w_b\langle\varphi_b|\varphi_a\rangle\varphi_b\int \frac{\nabla K(\boldsymbol{r} - \boldsymbol{q}_a) \cdot \nabla K(\boldsymbol{r} - \boldsymbol{q}_b)}{\sum_c w_c K(\boldsymbol{r} - \boldsymbol{q}_c)}\,\mathrm{d}^3 r\,. \tag{24}$$

We remark that the present treatment is inherently nonadiabatic, and there seems to be no clear sense in which certain terms in equation (24) are particularly responsible for the nonadiabatic coupling terms appearing in Born-Huang expansions. Indeed, even if we were to drop the last term in (22), we would recover the nonadiabatic mean-field model. However, the last term in (22) is essential in that it retains the nonlocal quantum features occurring in bohmion dynamics, so that the motion of each bohmion depends on all other bohmion locations. In this sense, since quantum aspects are retained for both the nuclear and the electronic motion, the bohmion method is a trajectory-based method while not exactly a mixed quantum-classical scheme. The latter can still be obtained by eliminating the nuclear quantum potential in the Lagrangian (18) by following the treatment developed in [15].

At this stage, the level of complication of these equations means it is difficult to make predictions concerning the main properties of the model. In the next section we will explore these properties in more detail by considering a series of numerical benchmark problems.

3 Results for model systems

In this section we compare the bohmion method with well-established ab-initio schemes including mean-field (Ehrenfest), trajectory surface hopping (TSH), and the coupled-trajectory mixed-quantum-classical method (CT-MQC) [4]; see Appendix B. We do this by testing bohmions on four model systems, including the three so-called *Tully models*, Tully I,II,III.

The Tully models were first introduced in the 90s [49] and since then have become a standard testing ground for any new approach to nonadiabatic molecular dynamics. These simple two-state models with a one-dimensional nuclear degree of freedom enable exact quantum mechanical simulations to be performed against which approximate schemes may be compared. At the same time, the Tully models can mimic realistic higher-dimensional nonadiabatic molecular processes. For example, parallels can be drawn between Tully I and the photoisomerization of ethylene (as well as many other photodynamical processes), and similar comparisons can be made for the other Tully models [27].

To facilitate direct comparison with other nonadiabatic molecular dynamics schemes, we use the same initial conditions as those considered in [4]. In each case, we prepare a nuclear wavepacket at spatial infinity on the lowest BO electronic potential energy surface, then study what happens as it encounters a region of nonadiabatic coupling. Specifically, we are interested in whether bohmion dynamics accurately capture BO population transfer and electronic decoherence.

We work in atomic units from now on. All models considered here are two-state models with a one-dimensional nuclear coordinate r and molecular Hamiltonian given by

$$\widehat{H} = -\frac{1}{2M}\partial_r^2 + \widehat{H}_e\left(r\right) \tag{25}$$

featuring the electronic Hamiltonian (in a diabatic basis)

$$\hat{H}_e\left(r\right) = \begin{pmatrix} H_{11}\left(r\right) & H_{12}\left(r\right) \\ H_{21}\left(r\right) & H_{22}\left(r\right) \end{pmatrix}. \tag{26}$$

3.1 Tully I (single avoided crossing)

Tully I is defined by the electronic matrix elements

$$H_{11}(r) = a\,[1 - \exp(-br)], \quad r > 0, \tag{27}$$

$$H_{11}(r) = -a\,[1 - \exp(br)], \quad r < 0, \tag{28}$$

$$H_{22}(r) = -H_{11}(r), \tag{29}$$

$$H_{12}(r) = H_{21}(r) = c\exp\left(-dr^2\right) \tag{30}$$

with $a = 0.01, b = 1.6, c = 0.005, d = 1.0$. The BO energy surfaces are illustrated in Figure 1. Note that there is a single avoided crossing, centred at $r = 0$. When the nuclear wavepacket
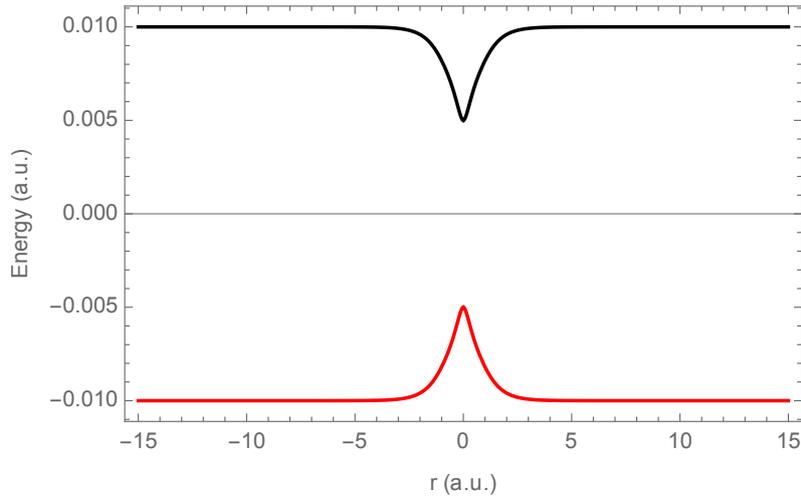

Figure 1: Tully I BO energy surfaces.

(coming in from spatial infinity on the lowest BO electronic state) encounters this avoided crossing, some nonadiabatic transitions into the upper BO state occur. The wavepacket then branches (see Figure 3), with the lower BO wavepacket moving faster than the upper BO wavepacket.

Recall that the bohmion method involves the introduction of a mollifier, which we take to be a Gaussian filter (with some width α) in all of our simulations. In general, one expects the accuracy of the method to improve as $\alpha \to 0$, though in practice this requires more bohmions (larger N) to achieve reasonable convergence of the results. It should be noted that another difficulty in taking α to be very small can arise, as follows. To understand this difficulty, recall that the regularized quantum potential represents a non-local interaction potential for the bohmions which has characteristic energy scale $\mathcal{E} = \hbar^2/M\alpha^2$, as can be seen from the second line of (22) when K is taken to be a Gaussian of width α. Consequently, for small α, we expect the electronic density matrix elements to oscillate with frequency $\omega \sim \hbar/M\alpha^2$ whose growth as α^{-2}, can impose very small timestep requirements in our numerical algorithm. In each plot we indicate our final choice for α and N. See Figure 6 in Section 3.2 for the dependence of the results on α.

We run two simulations for Tully I, with the nuclear wavepacket given initial momenta $k = 10$ and $k = 25$ respectively. In Figure 2 we plot the BO populations and coherence measure in both cases. For the choice $\alpha = 1/20$, the plots are already in good agreement with exact results; see Figure 11 in Appendix B. Particularly noteworthy is the accurate capture
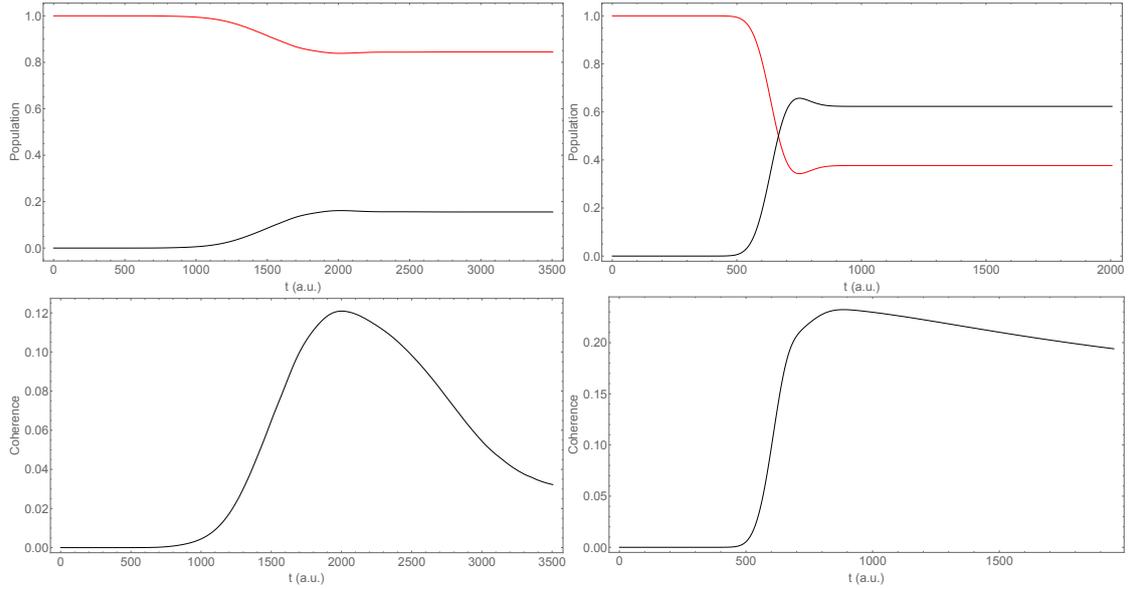
Figure 2: BO populations and coherence for Tully I. Left: $k = 10$, $N = 4000$, $\alpha = 1/20$. Right: $k = 25$, $N = 1000$, $\alpha = 1/20$.

of decoherence, a phenomena which many traditional methods such as TSH and Ehrenfest completely fail to capture for this model. The CT-MQC method captures decoherence to some extent [4], but not as accurately as the bohmion method manages to do here.

Another important effect accurately captured by the bohmion method is nuclear wavepacket splitting. In Figure 3 we show snapshots of the nuclear density and BO projections during the course of the $k = 10$ simulation. We see that the nuclear wavepacket ultimately splits into two wavepackets, one located on the lower BO surface and one on the higher BO surface. The latter wavepacket moves slower than the former, and so the two move apart as one would expect.
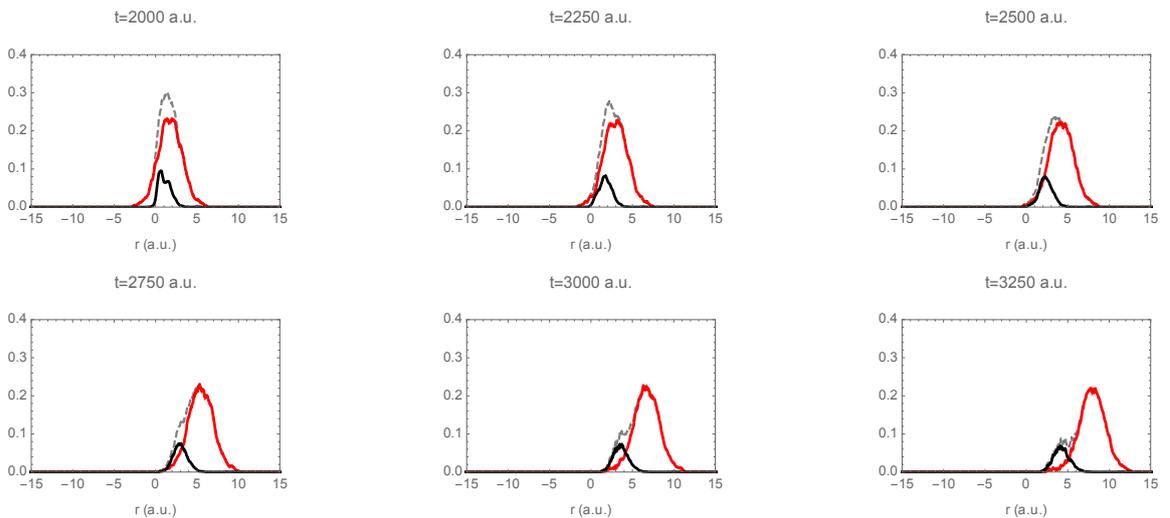
Figure 3: Wavepacket splitting in Tully I. $k = 10$, $N = 4000$, $\alpha = 1/20$. In each snapshot, the dotted line represents the regularized probability density $\bar{D}(r, t) = \int K(r - r')D(r', t)\,dr$. The red and black lines represent the populations of the lower and upper BO surfaces respectively, which are computed from the regularized density matrix density $\bar{\rho}(r, t) = \int K(r - r')\tilde{\rho}(r', t)\,dr$.

This behaviour is missed by schemes based on independent nuclear trajectories. For example, in Ehrenfest dynamics the ultimate fate of a trajectory is that it follows a potential energy surface which is some weighted average of the two BO surfaces (rather than one or the other), and so nuclear wavepacket splitting of this sort is impossible [49]. Thus, the coupling between the bohmion trajectories, through the (regularized) quantum potential, is therefore crucial in capturing this effect.

3.2 Tully II (dual avoided crossing)

Tully II is defined by the electronic matrix elements

$$H_{11}(r) = 0, \tag{31}$$

$$H_{22}(r) = -a \exp\left(-br^2\right) + e_0, \tag{32}$$

$$H_{12}(r) = H_{21}(r) = c \exp\left(-dr^2\right) \tag{33}$$

with $a = 0.1, b = 0.28, c = 0.015, d = 0.06, e_0 = 0.05$. The BO energy surfaces are illustrated in Figure 4. Note that there are two avoided crossings, located either side of $r = 0$. When
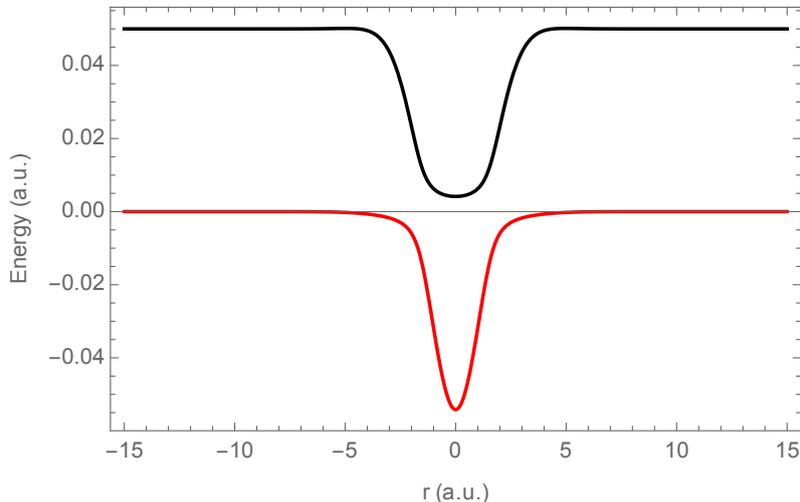
Figure 4: Tully II BO energy surfaces.

the nuclear wavepacket (coming in from spatial infinity on the lowest BO electronic state) encounters the first avoided crossing, some nonadiabatic transitions into the upper BO state occur and the wavepacket branches as in Tully I. The wavepackets then encounter the second avoided crossing at which further transitions occur. The wavepackets can recombine at this point leading to interference effects whose strength depends on the momentum of the initial wavepacket [49]. It was recently pointed out that a molecular analogue of Tully II, whose dynamics are characterized by multiple crossings between electronic states, can be found in the photodynamics of the molecule DMABN [27].

We run two simulations, with the nuclear wavepacket given initial momenta $k = 16$ and $k = 30$ respectively. In Figure 5 we plot the BO populations and coherence measure in both cases. We also show the effect of changing the regularization lengthscale α in Figure 6.

Once again, upon comparing with Figure 11 in Appendix B, the decoherence is captured excellently by the bohmions, far better than any of the traditional methods, including CT-MQC. Another impressive feature of the bohmion dynamics is the population transfer for the
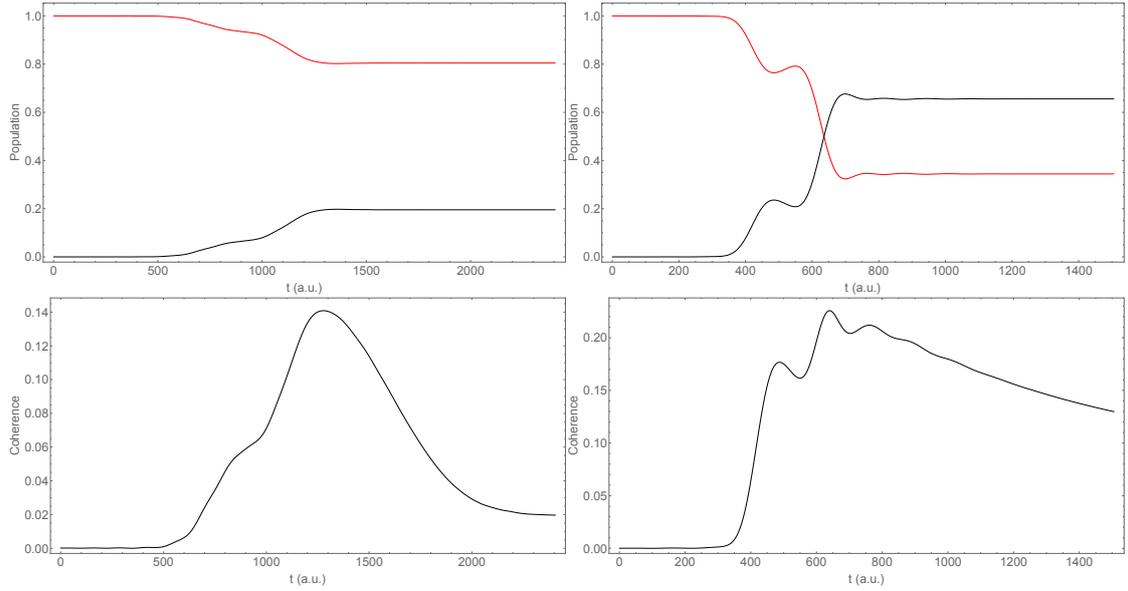
Figure 5: BO populations and coherence for Tully II. Left: $k = 16$, $N = 4000$, $\alpha = 1/20$. Right: $k = 30$, $N = 1000$, $\alpha = 1/20$.

lower momentum ($k = 16$) scattering. The bohmion model captures the final BO populations with high accuracy, in contrast to all other traditional methods which appear to struggle to capture the dynamics of the passage through the second avoided crossing. No such problem is encountered by the bohmions, and the final BO population for the lowest BO surface is lower than that found by TSH, Ehrenfest, and MQC methods, in agreement with exact quantum mechanical results.
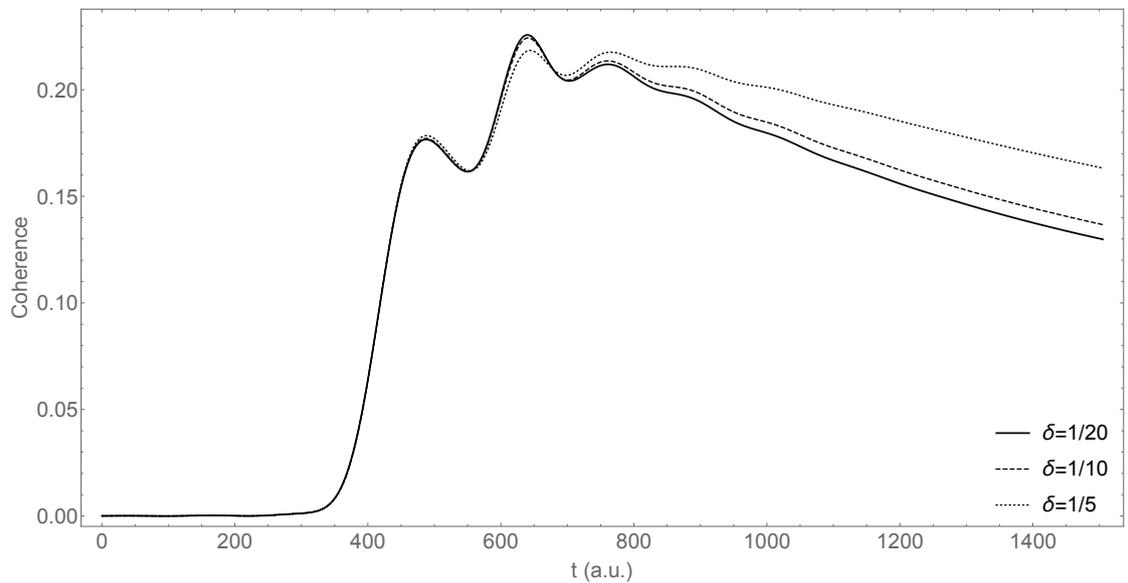
Figure 6: Coherence for Tully II. $k = 30$, $N = 1000$, for varying regularization lengthscale α.

3.3   Tully III (extended coupling region with reflection)

Tully III is defined by the electronic matrix elements

$$H_{11}(r) = -H_{22}(r) = a, \tag{34}$$

$$H_{12}(r) = b\left[2 - \exp(-cr)\right], \quad r > 0, \tag{35}$$

$$H_{12}(r) = b\exp(cr), \quad r < 0, \tag{36}$$

$$H_{12}(r) = H_{21}(r) \tag{37}$$

with $a = 0.0006, b = 0.1, c = 0.9$. The BO energy surfaces are illustrated in Figure 7. The
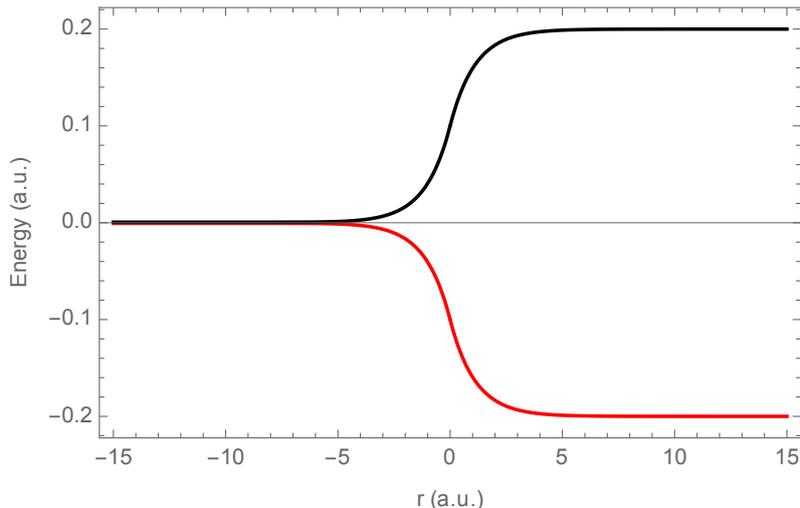
Figure 7: Tully III BO energy surfaces.

nuclear wavepacket first encounters an extended coupling region ($r < 0$), where the two BO energy surfaces are very close together, before the BO surfaces move apart. The wavepacket branches at this point, and (depending on the initial momentum) the part on the upper BO surface can be reflected if it doesn't have sufficient energy to climb the potential barrier. This reflected wavepacket then encounters the extended coupling region for a second time. It was suggested in [27] that these dynamics, involving a reflection process which leads to a second passage through a region of nonadiabatic coupling, are paralleled to some extent in the nonradiative deactivation of fulvene.

We run two simulations, with the nuclear wavepacket given initial momenta $k = 10$ and $k = 30$ respectively. In Figure 8 we plot the BO populations and coherence measure in both cases. The bohmion simulations perform very well for the higher momentum case $k = 30$, again capturing the decoherence with greater accuracy than the other methods we have been discussing; see Figure 11 in Appendix B. The lower momentum simulation involves more challenging dynamics, with significant wavepacket splitting and reflection. The results shown in Figure 8, computed with a regularization lengthscale of $\alpha = 1/20$ a.u., successfully capture the correct qualitative behaviour of the coherence measure throughout, although losing some accuracy at later times > 3000 a.u. when the reflected wavepacket re-enters the extended coupling region.

More accurate results can in principle be obtained by choosing a smaller regularization lengthscale α, as discussed earlier. However, descreasing the regularization lengthscale α comes at the cost of increasing the number of bohmions and requiring a smaller timestep. In practice
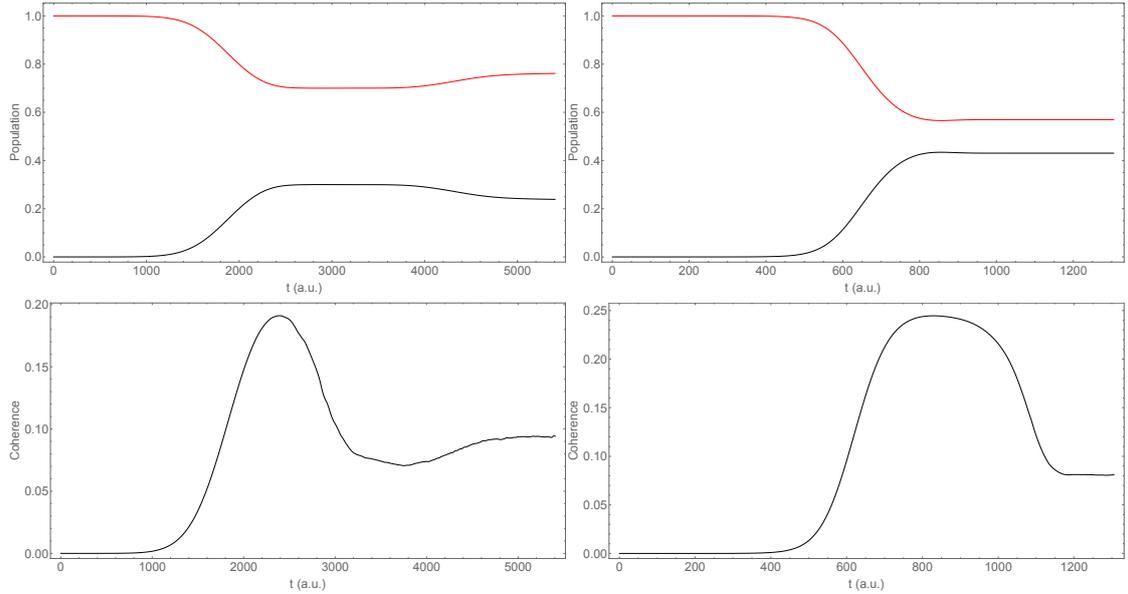
Figure 8: BO populations and coherence for Tully III. Left: $k = 10$, $N = 4000$, $\alpha = 1/20$. Right: $k = 30$, $N = 2000$, $\alpha = 1/30$.

we find that the latter is the principle limitation, because our numerical method (based on a fixed timestep Runge-Kutta scheme) eventually loses stability for much smaller α. It would be worth investigating whether this situation could be improved by using an adaptive scheme.

3.4 Double Arch model

The Double Arch model is defined by the electronic matrix elements

$$H_{11}(r) = -H_{22}(r) = a, \tag{38}$$
$$H_{12}(r) = -b \exp(c(r-d)) + b \exp(c(r+d)), \quad r < -d, \tag{39}$$
$$H_{12}(r) = b \exp(-c(r-d)) - b \exp(-c(r+d)), \quad r > d, \tag{40}$$
$$H_{12}(r) = 2b - b \exp(c(r-d)) - b \exp(-c(r+d)), \quad -d < r < d, \tag{41}$$
$$H_{21}(r) = H_{12}(r) \tag{42}$$

with $a = 0.0006, b = 0.1, c = 0.9, d = 4$. The BO energy surfaces are illustrated in Figure 9. As in Tully III, after a region of extended coupling the BO surfaces move apart. In this model, they then come together again for a second region of extended coupling, forming a double arch shape.

We run two simulations, with the nuclear wavepacket given initial momenta $k = 20$ and $k = 40$ respectively. In Figure 10 we plot the BO populations and coherence measure in both cases. Upon comparing again with Figure 11, we see that the quality of agreement is similar to Tully III: the correct qualitative behaviour is seen throughout the simulations, though with a loss of accuracy, particularly for the lower momentum case ($k = 20$) at later times ($t > 1000$). We emphasise, though, that the agreement is at least as good as all the other methods we have been considering (CT-MQC is the only other method capturing the right qualitative behaviour) and the bohmions once again display superior accuracy at early times.

14
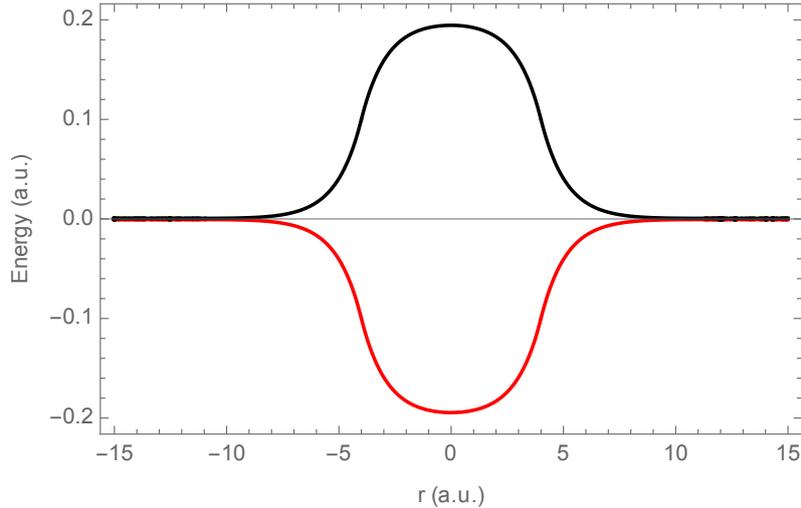
Figure 9: Double Arch model BO energy surfaces.
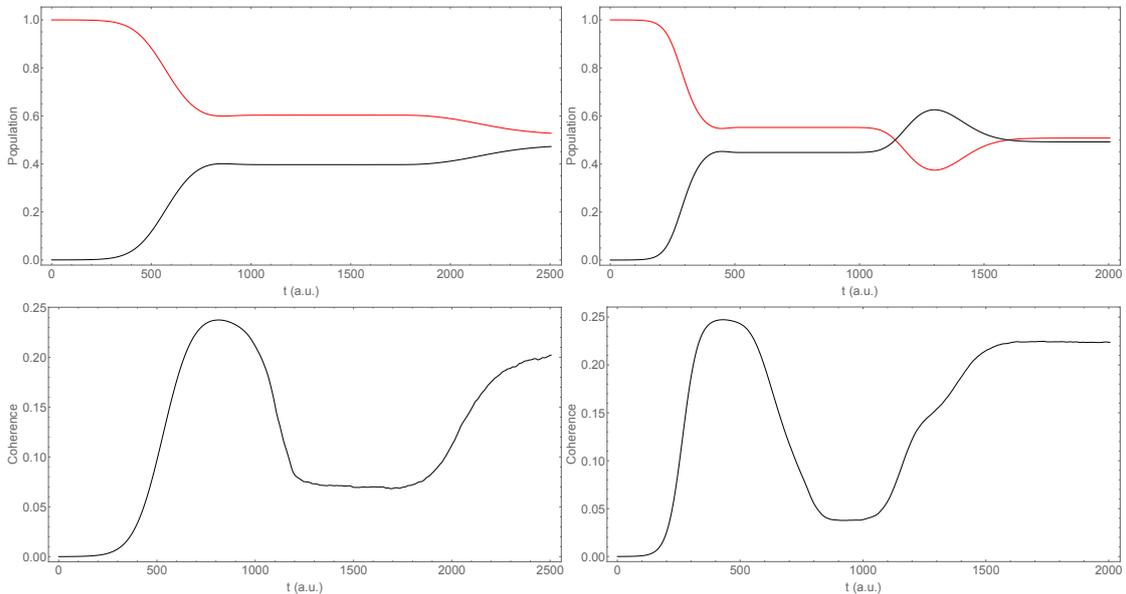
Figure 10: BO populations and coherence for Double Arch model. Left: $k = 20$, $N = 2000$, $\alpha = 1/30$. Right: $k = 40$, $N = 2000$, $\alpha = 1/30$.

4   Conclusions

In this work, we have applied the recently developed bohmion method to the celebrated Tully models of nonadiabatic molecular dynamics, allowing direct comparison with other approximate schemes. These other schemes included Ehrenfest, TSH and CT-MQC, as well as the exact quantum mechanical results. Although the Tully models are simple, they have enabled us to assess the extent to which these methods can accurately capture essential features of nonadiabatic dynamics such as population transfer and electronic decoherence.

Our simulations have demonstrated that the bohmion method, on the whole, captures electronic decoherence with far better accuracy than the other methods mentioned above. This is a very promising result, as the correct capture of electronic decoherence effects remains

a great challenge in the field of quantum-classical coupling. The bohmion method, being based on the exact factorization of the molecular wavefunction, retains correlations between the electrons and nuclei which are crucial to the decoherence dynamics through the inclusion of the (regularized) quantum potential, a non-local interaction potential which depends on the positions of all the bohmions.

Bohmions performed best on Tully I and Tully II, with a loss of accuracy in the case of Tully III which involves wavepacket reflection at low wavepacket momenta. Greater accuracy should be obtainable by performing the simulations with a smaller regularization lengthscale α, although this may require a more sophisticated numerical scheme in order to resolve numerical instabilities. Still, the correct qualitative behaviour is captured by the bohmions, even for this most challenging model.

We point out that the results in [4] were obtained with a few hundred trajectories while our implementation involved a few thousand bohmions. In our work, these large numbers were chosen for accuracy purposes. Indeed, we observed in our simulations that a few hundred bohmions were sufficient to account for effects such as wavepacket reflection (in Tully III) even if with some loss of accuracy.

These one-dimensional results seem very promising. A natural next step would be to investigate the application of the bohmion method to higher dimensional problems, including molecules in their full dimensionality. The evaluation of the regularised quantum potential poses a challenge in this respect, because it is given by an integral over the (potentially high-dimensional) nuclear coordinate space which will likely require Monte Carlo methods.

A   Numerical details

The equations of motion for the bohmion trajectories (in the case of a one-dimensional model) can be equivalently expressed as canonical Hamilton's equations

$$\dot{q}_a = \frac{\partial H}{\partial p_a}, \qquad \dot{p}_a = -\frac{\partial H}{\partial q_a} \tag{43}$$

for the Hamiltonian

$$H(\{q\}, \{p\}, \{\varrho\}) = \sum_a \left[\frac{p_a^2}{2 w_a M} + w_a \langle \varrho_a | \widehat{H}_e(q_a) \rangle \right.$$

$$\left. + \frac{\hbar^2}{8M} \sum_b w_a w_b \left(2 \langle \varrho_a | \varrho_b \rangle - 1 \right) \int \frac{K'(r - q_a) K'(r - q_b)}{\sum_c w_c K(r - q_c)} \, \mathrm{d}r \right]. \tag{44}$$

These equations are to be integrated together with the electronic equation (23). In our simulations, conservation of H has been used as a test for the quality of convergence of our numerical

16

scheme. We integrate these equations of motion using a fourth-order Runge-Kutta scheme with a step size of $t = 0.5$ a.u. and, following previous work, we take $M = 2000$ a.u. This value of M is comparable to the proton mass.

At each timestep, integrals over the nuclear coordinate space must be evaluated, corresponding to the final term in the above Hamiltonian. This evaluation is accomplished by using a simple trapezoidal rule with a sample spacing of $\alpha/3$, where α is the width of the Gaussian filter K used to regularize the quantum potential. We integrate within a finite box with variable size determined by the positions of the right-most and left-most bohmions. For higher dimensional problems one should use Monte Carlo methods, as these have better scaling properties. We have verified that the one-dimensional integrals appearing here can indeed be accurately evaluated by Monte Carlo methods.

The electronic density matrix is evaluated as

$$\rho_e\left(x, x'\right) = \int D(r)\phi(r)\phi^*(r)\,\mathrm{d}r = \int \sum_{a=1}^{N} w_a \varrho_a\left(t\right) \delta\left(r - q_a\left(t\right)\right) \mathrm{d}r = \sum_{a=1}^{N} w_a \varrho_a\left(t\right) \tag{45}$$

while the BO populations can be evaluated as

$$\sum_{a=1}^{N} w_a \left\langle \psi^{(i)}(q_a(t)) \right| \varrho_a(t) \left| \psi^{(i)}(q_a(t)) \right\rangle \tag{46}$$

with $\left| \psi^{(i)}\left(q_a\left(t\right)\right) \right\rangle$ ($i = 1$ or 2) the relevant BO electronic wavefunction. Following previous work, we take our coherence measure to be given by

$$\sum_{a=1}^{N} w_a \left| \left\langle \psi^{(1)}(q_a(t)) \right| \varrho_a(t) \left| \psi^{(2)}(q_a(t)) \right\rangle \right|^2 \tag{47}$$

i.e. the modulus-squared of the off-diagonal term (in the adiabatic basis) of the electronic density matrix.

Following previous work, we take the initial nuclear wavepacket momentum k and width Δ to be related by $\Delta = 20\hbar/k$. The initial bohmion velocities $\dot{q}_a$ are all taken to be equal to the initial wavepacket velocity k/M, and the centre r_0 of the initial wavepacket is taken to be $r_0 = -8$ a.u. for the first two models and $r_0 = -15$ a.u. for the final two models.

We specify our initial bohmion positions by approximating the initial nuclear distribution

$$D\left(r, t\right) = \frac{1}{\Delta\sqrt{\pi}} \exp\left(-\left(\frac{r - r_0}{\Delta}\right)^2\right) \tag{48}$$

by a finite sum

$$D\left(r, t\right) = \sum_{a=1}^{N} w_a \delta(r - q_a(t)) \tag{49}$$

where we take the q_a to be sampled from a normal distribution, centre r_0 and width Δ, and we pick the weights w_a to all be equal with $\sum_{a=1}^{N} w_a = 1$. Sampling was performed with a *pseudo*random number generator and also with a *quasi*random number generator based on an inverse CDF transform of the one-dimensional Sobol sequence, with both methods giving accurate results. The results presented here use the quasirandom sampling method, for which we found faster convergence as the number of trajectories was increased. This is not surprising: the convergence properties of Monte Carlo and quasi-Monte Carlo methods are well-studied and the scaling of quasi-Monte Carlo methods (with numbers of samples, but also with dimensionality [42]) is known to be superior, at least asymptotically.

B Comparison with other methods

Here, we display the results obtained on the Tully models by using other methods; see Figure 11. In particular, we consider the Ehrenfest mean-field method (MF), the trajectory surface-hopping (TSH), and two variants of the mixed quantum-classical method (MQC and CT-MQC). These plots appeared in reference [4] and are presented here for comparison.
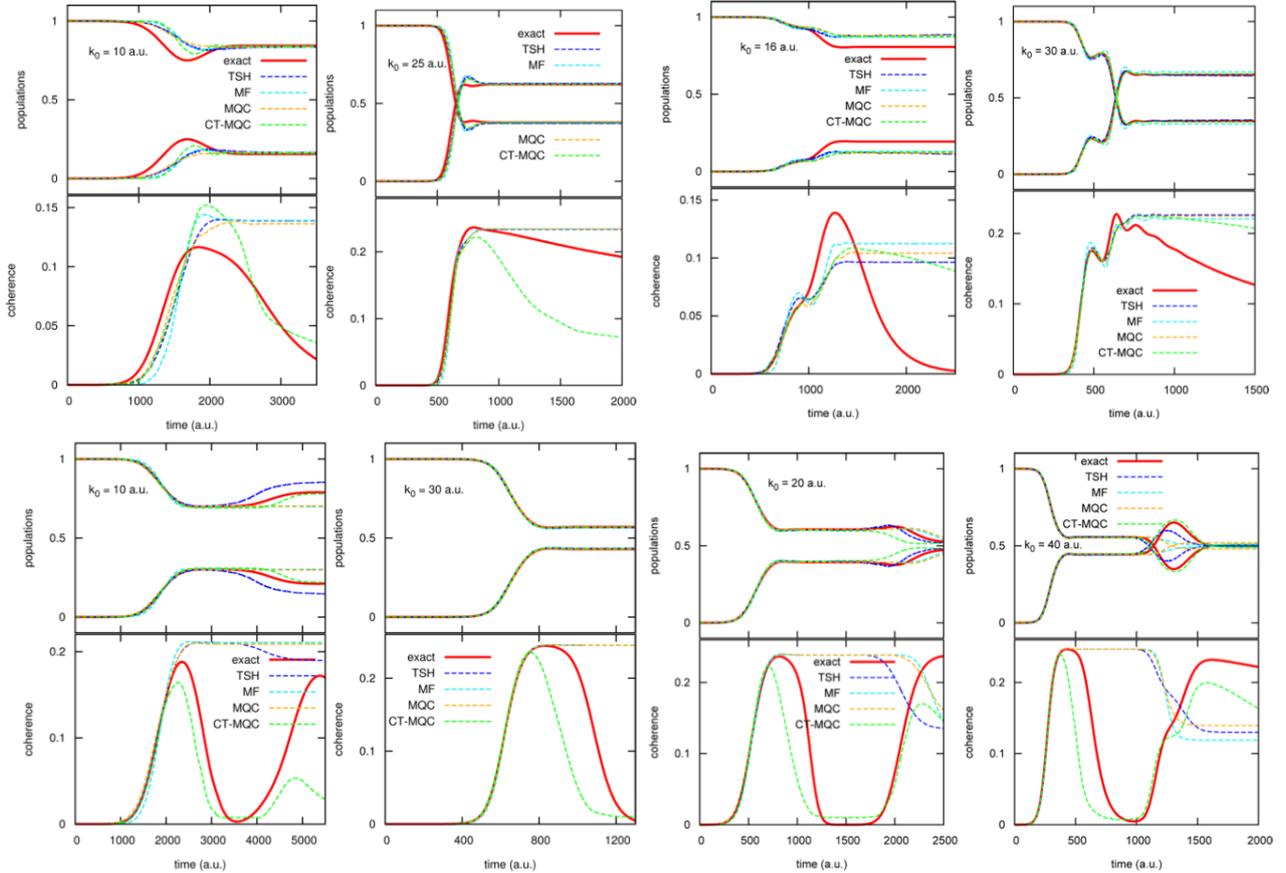

Figure 11: Results for (left to right; top to bottom) model (a), (b), (c) and (d). Reprinted (adapted) with permission from F. Agostini, S. K. Min, A. Abedi, E. K. U. Gross, J. Chem. Theory Comput. 12 (2016), n. 5, 2127-2143. Copyright 2016 American Chemical Society.

References

[1] Abedi, A., Maitra, N. T. and Gross, E. K. U. *Correlated electron-nuclear dynamics: Exact factorization of the molecular wavefunction.* J. Chem. Phys. 137 (2012), n. 22, 22A530

[2] Abedi, A.; Maitra, N. T.; Gross, E. K. U. *Exact factorization of the time-dependent electron-nuclear wave function.* Phys. Rev. Lett. 105 (2010), 12, 123002

[3] Agostini, F.; Caprara, S.; Ciccotti, G. *Do we have a consistent non-adiabatic quantum-classical mechanics?* Eur. Phys. Lett. 78 (2007), n. 3, 30001

[4] Agostini, F.; Min, S. K.; Abedi, A.; Gross, E. K. U. *Quantum-Classical Nonadiabatic Dynamics: Coupled- vs Independent-Trajectory Methods.* J. Chem. Theory Comput. 12 (2016), n. 5, 2127-2143

[5] Ben-Nun, M.; Martínez, T. J. *Nonadiabatic molecular dynamics: validation of the multiple spawning method for a multidimensional problem.* J. Chem. Phys. 108 (1998), n. 17, 7244-7257

[6] Bialynicki-Birula, I.; Cieplak, M.; Karminski, J.; Furdyna, A.M. Theory of Quanta. Oxford University Press. 1992

[7] Bondar, D.I.; Gay-Balmaz, F.; Tronci, C. *Koopman wavefunctions and classical-quantum correlation dynamics.* Proc. R. Soc. A. 475 (2019), n. 2229, 20180879

[8] Bonet-Luz, E.; Tronci, C. *Geometry and symmetry of quantum and classical-quantum variational principles.* J. Math. Phys. 56 (2015), 082104

[9] Born, M.; Huang, K. Dynamical Theory of Crystal Lattices; Clarendon: Oxford, UK, 1954.

[10] Born, M. and Oppenheimer, R. *Zur quantentheorie der molekeln.* Ann. Physik, 389 (1927), n. 20, 457-484.

[11] de Carvalho, F.F.; Bouduban, M.E.F.; Curchod, B.F.E.; Tavernelli, I. *Nonadiabatic molecular dynamics based on trajectories.* Entropy, 16 (2014), 62-85.

[12] Crespo-Otero, R.; Barbatti, M. *Recent advances and perspectives on nonadiabatic mixed quantum-classical dynamics.* Chem. Rev. 118 (2018), n. 15, 7026-7068

[13] Curchod, B. F. E.; Tavernelli, I.; Rothlisberger, U. *Trajectory-based solution of the nonadiabatic quantum dynamics equations: an on-the-fly approach for molecular dynamics simulations.* Phys. Chem. Chem. Phys. 13 (2011), n. 8, 3231-3236

[14] Foskett, M.S. Geometry of Quantum Hydrodynamics in Theoretical Chemistry. PhD thesis. University of Surrey. 2020.

[15] Foskett, M.S.; Holm, D.D.; Tronci, C. *Geometry of nonadiabatic quantum hydrodynamics.* Acta Appl. Math. 162 (2019), 1-41

[16] Foskett, M.S.; Tronci, C. *Holonomy and vortex structures in quantum hydrodynamics.* Math. Sci. Res. Inst. Publ. (to appear). arXiv:2003.08664

[17] Gay-Balmaz, F.; Tronci, C. *Madelung transform and probability densities in hybrid quantum-classical dynamics.* Nonlinearity 33 (2020), 5383-5424.

[18] Garashchuk, S.; Rassolov, V.; Prezhdo, O. *Semiclassical Bohmian dynamics.* Rev. Comp. Chem. 27 (2010), 287-368

[19] Granucci, G.; Persico, M.; Zoccante, A. *Including quantum decoherence in surface hopping.* J. Chem. Phys. 133 (2010), n. 13, 134111

[20] Huber, D.; Heller, E.J. *Hybrid mechanics, a combination of classical and quantum mechanics.* J. Chem. Phys. 89 (1988), n. 8, 4752-4760

[21] Hunter, G. *Conditional probability amplitudes in wave mechanics.* Int. J. Quant. Chem. 9 (1975), 237-242

[22] Holm, D.D. Geometric Mechanics. I & II. Imperial College Press. 2011

[23] Holm, D.D.; Marsden, Momentum maps and measure valued solutions (peakons, filaments, and sheets) of the Euler-Poincaré equations for the diffeomorphism group. In *The Breadth of Symplectic and Poisson Geometry, A Festshrift for Alan Weinstein*, 203-235, *Progr. Math.*, **232**, J.E. Marsden and T.S. Ratiu, Editors, Birkhäuser Boston, Boston, MA, 2004. https://doi.org/10.1007/0-8176-4419-9_8

[24] Holm, D.D.; Marsden, J.E.; Ratiu, T.S. *The Euler-Poincaré equations and semidirect products with applications to continuum theories.* Adv. Math. 137 (1998), n. 1, 1-81.

[25] Holm, D. D. and Tronci, C., 2009. Geodesic flows on semidirect-product Lie groups: geometry of singular measure-valued solutions. *Proc. Royal Society of London A*, 465 (2102): 457-476.

[26] Huber, D.; Heller, E.J. *Hybrid mechanics, a combination of classical and quantum mechanics.* J. Chem. Phys. 89 (1988), n. 8, 4752-4760

[27] Ibele, L. M.; Curchod, B. F. E. *A molecular perspective on Tully models for nonadiabatic dynamics.* Phys. Chem. Chem. Phys. 22 (2020), 15183

[28] Joubert-Doriol, L.; Izmaylov, A.F. *Nonadiabatic quantum dynamics with frozen-width Gaussians.* J. Phys. Chem. A 122 (2018), n. 29, 6031-6042

[29] Kapral R. *Progress in the theory of mixed quantum-classical dynamics.* Annu. Rev. Phys. Chem. 57 (2006), 129–157.

[30] Kramer, P.; Saraceno, M. Geometry of the Time-Dependent Variational Principle in Quantum Mechanics. Springer-Verlag Berlin Heidelberg. 1981

[31] Madelung, E.: Eine anschauliche Deutung der Gleichung von Schrödinger. Naturwissenschaften 14(45), 1004 (1926)

[32] Madelung, E.: Quantentheorie in hydrodynamischer Form. Z. Phys. 40(3?4), 322?326 (1927)

[33] Makhov, D. V.; Glover, W. J.; Martinez, T. J.; Shalashilin, D. V. *Ab initio multiple cloning algorithm for quantum nonadiabatic molecular dynamics.* J. Chem. Phys. 141 (2014), n. 5, 054110

[34] Marsden, J.E., Ratiu, T.S.: Introduction to Mechanics and Symmetry: A Basic Exposition of Classical Mechanical Systems. Springer, New York (2013)

[35] Marx, D.; Hutter, J. *Ab initio molecular dynamics: basic theory and advanced methods.* Cambridge University Press. (2009).

[36] Mead, A.C. *The geometric phase in molecular systems.* Rev. Mod. Phys. 64 (1992), n. 1, 51-85

[37] Prezhdo, O. V. *Mean field approximation for the stochastic Schrödinger equation.* J. Chem. Phys. 111 (1999), n. 18, 8366-8377

[38] Prezhdo, O. V.; Brooksby, C. *Quantum backreaction through the bohmian particle.* Phys. Rev. Lett. 86 (2001), n. 15, 3215-3219

[39] Provost, J.; Vallee, G. *Riemannian structure on manifolds of quantum states.* Comm. Math. Phys. 76 (1980), 289-301

[40] Rawlinson, J.I.; Tronci, C. *Regularized Born-Oppenheimer molecular dynamics.* Phys. Rev. A 102 (2020), n. 3, 032811

[41] Shalashilin, D. V. *Quantum mechanics with the basis set guided by Ehrenfest trajectories: Theory and application to spin-boson model.* J. Chem. Phys. 130 (2009), n. 24, 244101

[42] Shalashilin, D. V.; Child, M. S. *Description of tunneling with the help of coupled frozen Gaussians.* J. Chem. Phys. 114 (2001), 21

[43] Shalashilin, D.V.; Child, M.S. *The phase space CCS approach to quantum and semiclassical molecular dynamics for high-dimensional systems.* Chem. Phys. 304 (2004), 103-120

[44] Subotnik, J. E.; Jain, A.; Landry, B.; Petit, A.; Ouyang, W.; Bellonzi, N. *Understanding the surface hopping view of electronic transitions and decoherence.* Ann. Rev. Phys. Chem. 67 (2016), 387-417.

[45] Sudarshan, E.C.G. *Interaction between classical and quantum systems and the measurement of quantum observables.* Prāmaṇa 6 (1976), 117-126

[46] Suzuki, Y.; Watanabe, K. *Bohmian mechanics in the exact factorization of electron-nuclear wave functions.* Phys. Rev. A 94 (2016), n. 3, 032517

[47] Tavernelli, I. *Ab initio-driven trajectory-based nuclear quantum dynamics in phase space.* Phys. Rev. A 87 (2013), n. 4, 042501

[48] Tronci, C. *Momentum maps for mixed states in quantum and classical mechanics.* J. Geom. Mech. 11 (2019), no. 4, 639-656.

[49] Tully, J. C. *Molecular dynamics with electronic transitions.* J. Chem. Phys. 93 (1990), n. 2, 1061-1071

[50] Tully, J.C. *Nonadiabatic dynamics.* In "Modern Methods for Multidimensional Dynamics Computations in Chemistry" (D.L. Thompson ed.). World Scientific. Singapore. 1998.

[51] Tully, J. C.; Preston, R. K. *Trajectory surface hopping approach to nonadiabatic molecular collisions: the reaction of* H^+ *with* D_2. J. Chem. Phys. 55 (1971), n. 2, 562-572